Coseismic Faulting Complexity of the 2019 M_w 5.7 Silivri Earthquake in the Central Marmara Seismic Gap, Offshore Istanbul

Fatih Turhan[†1], Diğdem Acarel[*†2], Vladimír Plicka[3], Marco Bohnhoff[4,5], Remzi Polat[1], and Jiří Zahradník[3]

Abstract

The submarine Main Marmara fault is overdue for an M > 7 earthquake in direct vicinity to the Istanbul megacity and the only segment of the right-lateral North Anatolian fault zone that has not been activated since 1766. On 26 September 2019, an M_w 5.7 earthquake occurred offshore Silivri (west of Istanbul), stimulating the discussions on a future major earthquake. The predominant faulting style for this pending earthquake remains enigmatic. Here, we study the coseismic rupture evolution of the 2019 Silivri earthquake and decipher the multitype-faulting aspects by a nonstandard approach. The event was dominated by a large compensated linear vector dipole component, of about −50%, that we interpret as a consecutive strike-slip and thrust double-couple episode, closely collocated in space and time. Because of local variations of the fault geometry at the eastern boundary of the central basin, crustal shortening and related thrust faulting are expected. A striking observation is the almost synchronous occurrence of both faulting types during a single earthquake. The earthquake complexity here is reported for the first time in the Sea of Marmara region and has to be considered in future rupture scenarios of an expected M > 7 event, with subsequent consequences for tsunami hazard and risk.

Cite this article as Turhan, F., D. Acarel, V. Plicka, M. Bohnhoff, R. Polat, and J. Zahradník (2022). Coseismic Faulting Complexity of the 2019 M_w 5.7 Silivri Earthquake in the Central Marmara Seismic Gap, Offshore Istanbul, *Seismol. Res. Lett.* **94**, 75–86, doi: 10.1785/0220220111.

Supplemental Material

Introduction

Resolving the geometry and segmentation of critically stressed offshore faults is challenging due to limited near-fault observations. However, determining the complexity and faulting style of future earthquakes in the presence of densely populated shorelines is crucial in quantifying the potential of seismic and tsunami hazard and subsequent risk. The submerged branch of the North Anatolian fault zone (NAFZ) in northwestern Turkey is an impeccable representative of such a setting (e.g., Şengör *et al.*, 2005). The NAFZ is an approximately 1200-km-long right-lateral continental transform plate boundary (Barka, 1992; Şengör *et al.*, 2005), accommodating the motion between the Anatolian and Eurasian plates with an average slip rate of 20–25 mm/yr (Reilinger *et al.*, 2006). The NAFZ runs as a single strike-slip fault and splits into two or more fault branches before entering the Sea of Marmara (SoM) region. The northern branch, hereafter referred to as the Main Marmara fault, holds most of the deformation and is dispersed into a complex zone with subbranches, offsets, and bends that resulted in basins and ridges beneath the SoM (Okay *et al.*, 2000; Armijo *et al.*, 2002; Bécel *et al.*, 2010; Şengör *et al.*, 2014). A series of historical earthquakes struck the SoM region (offshore Istanbul) in 1509, 1719, 1766, and 1894 with moment magnitudes between 7.0 and 7.4 (Ambraseys and Jackson, 2000; Bohnhoff *et al.*, 2016). The Main Marmara fault (MMF) extends between the ruptures of the 1912 M_w 7.4 Ganos and 1999 M_w 7.4 İzmit events. The MMF has not been activated in a major event since 1766, accumulating strain and considered to be overdue for a large (M > 7) earthquake (Fig. 1a). The probability of an M > 7.0 earthquake to occur by 2034 is ∼38% (Parsons, 2004). Following the 1999 İzmit earthquake, several studies were conducted in the SoM region, involving high-resolution multibeam bathymetry and multichannel seismic profiling to map the seafloor, fault geometry, and basin structures to better understand the fault morphology and kinematics (e.g., Parke *et al.*, 2002; Demirbağ

1. Kandilli Observatory and Earthquake Research Institute (KOERI), Regional Earthquake-Tsunami Monitoring Center (RETMC), Boğaziçi University, Istanbul, Turkey, https://orcid.org/0000-0003-4612-7421 (FT); 2. Institute of Earth and Marine Sciences, Gebze Technical University, Kocaeli, Turkey, https://orcid.org/0000-0002-3179-6342 (DA); 3. Faculty of Mathematics and Physics, Charles University, Prague, Czech Republic, https://orcid.org/0000-0002-3316-8825 (VP); https://orcid.org/0000-0002-1307-2957 (JZ); 4. Helmholtz Centre Potsdam, GFZ German Research Centre for Geosciences, Potsdam, Germany, https://orcid.org/0000-0001-7383-635X (MB); 5. Institute of Geological Sciences, Free University of Berlin, Berlin, Germany

*Corresponding author: dacarel@gtu.edu.tr

†These authors contributed equally to this work.

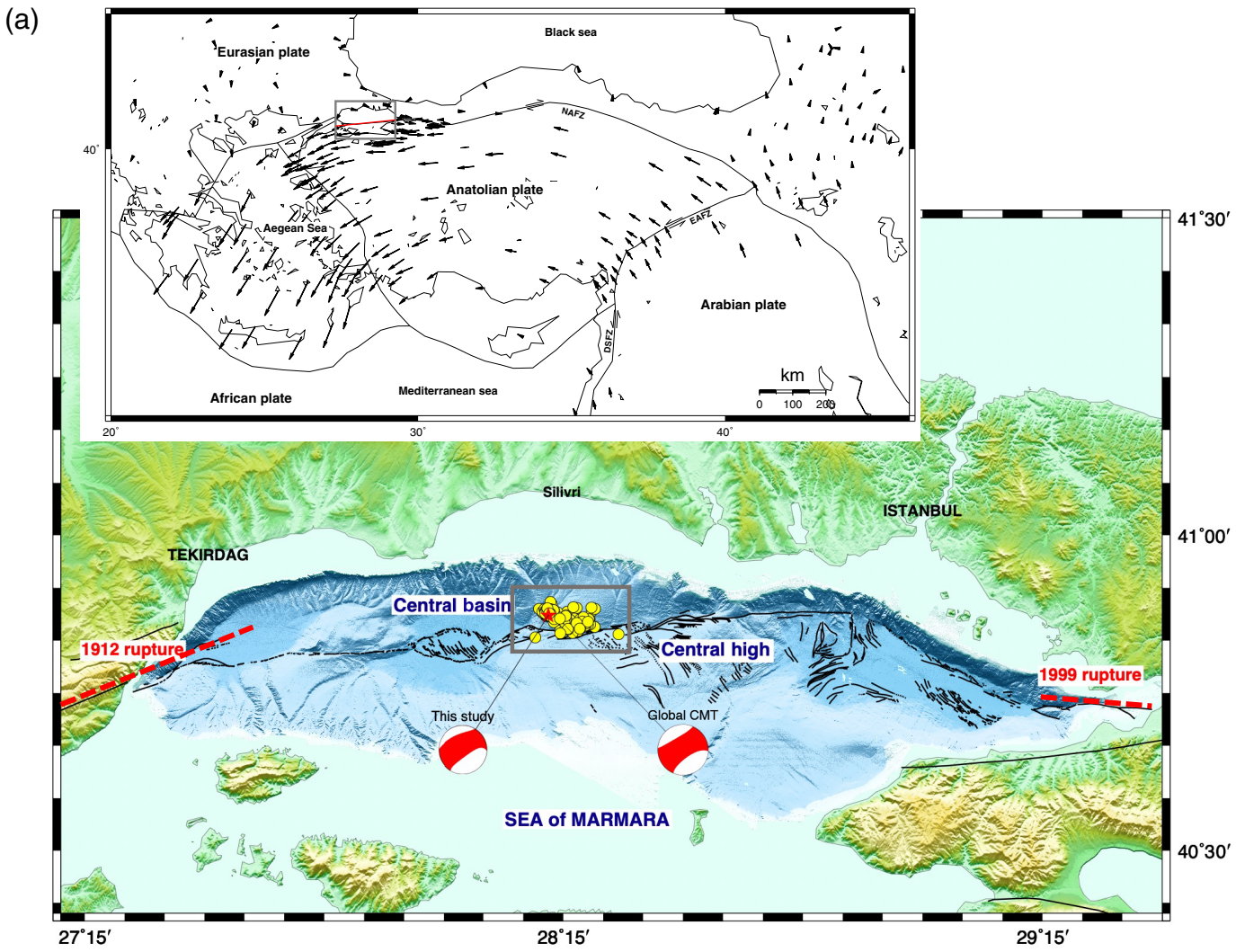

Figure 1. (a) The Sea of Marmara region in northwestern Turkey with major tectonic elements and the Main Marmara fault (MMF). Focal mechanisms of the mainshock determined in this study and by Global Centroid Moment Tensor (Global CMT) are shown in red. The yellow dots are epicentral locations of 127 events (M >2) occurring between 24 September 2019 and 11 January 2020. Ruptures of the recent regional M > 7 earthquakes (1912 and 1999) are plotted as red dashed lines. The MMF in between is overdue for an M > 7 event. The epicenter of the Silivri mainshock is denoted with a red star. (b) Multiple-point-source modeling of the mainshock in the frequency range of 0.03–0.08 Hz, projected onto a horizontal line grid located at 8 km depth. Trial points are shown in red diamonds. The best pair for a strike-slip subevent-1 and a thrust-fault subevent-2 from iterative deconvolution is presented by the focal mechanism symbols with sector shading. The rupture plane for subevent-1 (strike/dip/rake: 286/60/178, purple) and tentative rupture planes for subevent-2 (104/73/106 and 239/23/47 in pink and green, respectively) are plotted. The other rectangles (dashed) indicate the alternative rupture planes of subevent-2 with a fixed location of subevent-1. The focal mechanism symbols without sector shading represent the jackknife estimate of nodal line uncertainty. Focal mechanisms of earthquakes M > 4.0 calculated in this study are shown in gray. Inset: Tectonic map of Turkey and surroundings; MMF is shown in red. Global Positioning System (GPS) vectors are from Reilinger *et al.* (2006). DSFZ, Dead Sea fault zone; EAFZ, East Anatolian fault zone; NAFZ, North Anatolian fault zone. The color version of this figure is available only in the electronic edition.
(*Continued*)

et al., 2003; Rangin *et al.*, 2004; Laigle *et al.*, 2008; Gasperini *et al.*, 2021). Different conclusions were drawn, postulating a single thoroughgoing strike-slip fault versus a system of en-échelon normal faults (Le Pichon *et al.*, 2001; Armijo *et al.*, 2002). Nevertheless, deep fault geometry needs to be further identified because depth resolution is limited in multichannel seismic reflection studies. Deployment of temporary near-fault ocean bottom seismometer networks allows the increase of resolution locally (Sato *et al.*, 2004; Yamamoto *et al.*, 2017, 2020).

A key question is whether the overdue MMF is completely locked or partly creeping because this largely defines the seismic hazard and subsequent risk threatening Istanbul. Offshore

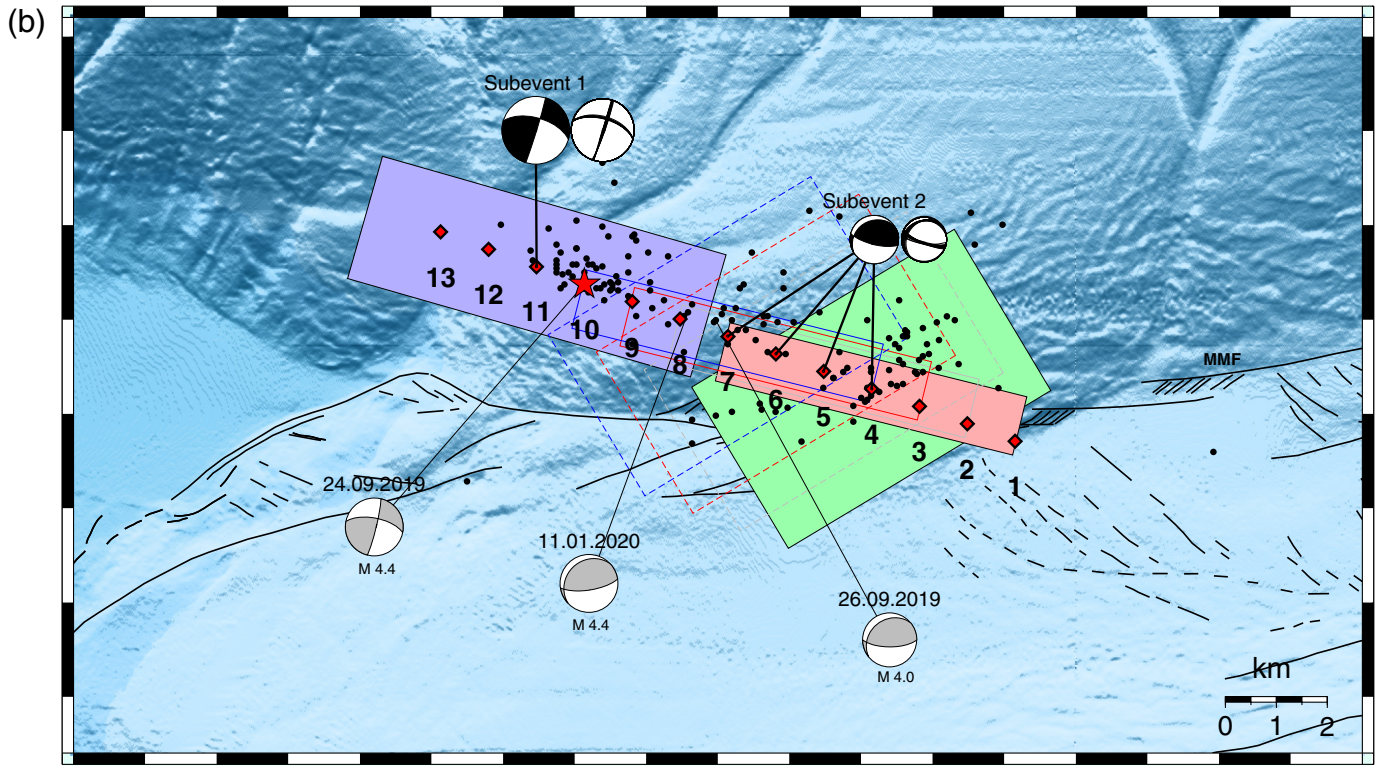

Figure 1. Continued

geodetic studies identified significant creep at the western part of the MMF (Yamamoto *et al.*, 2019), whereas a comparable study by Lange *et al.* (2019) identified a locked plate contact to the west of Istanbul. Onshore geodetic studies suggested a locked Ganos fault toward the west of the SoM region and also confirmed a locked status of the eastern part of the SoM region, immediately south of Istanbul (Ergintav *et al.*, 2014) as proposed earlier based on the absence of microseismicity (Bohnhoff *et al.*, 2013).

On 26 September 2019, an M_w 5.7 earthquake occurred on the MMF, offshore town of Silivri, at the transition from the partially creeping Central Basin (Ergintav *et al.*, 2014; Bohnhoff *et al.*, 2017) to the fully locked segment toward the east (Bohnhoff *et al.*, 2013; Schmittbuhl *et al.*, 2016; Lange *et al.*, 2019). The event triggered intense discussions on whether it reflects a preshock of a future major earthquake (Durand *et al.*, 2020; Irmak *et al.*, 2021; Karabulut *et al.*, 2021). It was also the largest regional earthquake since 1999. The event was preceded by a foreshock sequence, lasting four days including an M_w 4.4 earthquake, on 24 September 2019 (Durand *et al.*, 2020; Karabulut *et al.*, 2021). Generally, a right-lateral strike-slip regime is dominant in the SoM with normal-faulting components (e.g., Örgülü, 2011; Wollin *et al.*, 2018, 2019). However, some areas of transpression or thrust faulting confined in uplift areas and oblique shortening in parts of the basin margins are also identified (Wong *et al.*, 1995; Imren *et al.*, 2001; Le Pichon *et al.*, 2001; Armijo *et al.*, 2002; Hergert and Heidbach, 2011). The Silivri earthquake sequence epicenters map to the north of the MMF, in the region where inner and outer boundary faults coexist (Yamamoto *et al.*, 2020), indicating a complex fault network at depth rather than a single master strike-slip fault. The source mechanisms of the entire Silivri seismic sequence represent the general faulting characteristics of the MMF, that is, east–west-trending dextral strike-slip motion with a salient reverse component (Durand *et al.*, 2020; Karabulut *et al.*, 2021). According to Durand *et al.* (2020), the hypocenter locations of the Silivri sequence are not sufficiently resolved to discriminate whether only the principal fault or several collocated fault segments were activated. In contrast, Karabulut *et al.* (2021) state that a secondary fault beneath the sedimentary layers has been activated rather than the MMF itself, whereas Irmak *et al.* (2021) argue that a secondary thrust fault with a right-lateral strike-slip component hosted the Silivri mainshock. These studies have focused on the geometrical and tectonic aspects of the entire Silivri sequence by investigating the spatial distribution of events and the mainshock source process, assuming primarily the standard double-couple (DC) rupture models, either with a major strike-slip and a minor thrust component (Karabulut *et al.*, 2021) or vice versa (Irmak *et al.*, 2021). Accordingly, their kinematic slip models

used the standard assumption of a single-fault plane being activated during the event.

In this study, we focus on a less standard yet notable aspect, that the Silivri mainshock exhibited a significant non-double-couple (non-DC) part, particularly a large compensated linear vector dipole (CLVD) component, indicating a complex rupture process. The Global Centroid Moment Tensor (Global CMT—Dziewonski *et al.*, 1981; Ekström *et al.*, 2012) solution reported moment tensor with a negative CLVD component as large as −92%. In the past, due to limited data quality and quantity, earthquake source mechanisms were assumed to be pure DC. Nowadays, earthquakes with high non-DC components are successfully identified in geothermal and volcanic settings (i.e., Shuler *et al.*, 2013; Martínez-Garzón *et al.*, 2017; Cesca *et al.*, 2020; Hrubcová *et al.*, 2021), and active mining regions (Šílený and Milev, 2006; Julia *et al.*, 2009). For discussion of potential physical mechanisms of non-DC components, see Introduction section of Hrubcová *et al.* (2021).

Alternatively, a favorable explanation of a deviation from pure-shear dislocation can also be a complex faulting geometry, in which two or more 100% DC subevents occur simultaneously on a system of faults not restricted to any tectonic origin (Sipkin, 1986; Miller *et al.*, 1998; Lay *et al.*, 2013; Zhang *et al.*, 2017; Liu and Zahradník, 2020; Sokos *et al.*, 2020). In this study, we propose a similar interpretation for the Silivri earthquake concerning the submarine fault geometry along MMF. First, to avoid false non-DC components caused by inaccurate crustal models or noisy data (Frohlich, 1995; Julian *et al.*, 1998), we use the M_w 4.4 foreshock as a calibration event, proving its evident DC character. Second, by analyzing the Silivri mainshock with a similar setting, we obtain convincing evidence for a significant non-DC mechanism and analyze its uncertainty. Third, we interpret the observed CLVD component as a DC doublet, using three complementary methods (iterative deconvolution, joint search of source pairs, and analysis of first-motion polarities). Finally, we propose a tectonic explanation of our observation and discuss subsequent implications in a case of nontrivial strike-slip activation of MMF.

Toward Reliable Estimates of Non-DC Components

To elucidate the details of the source process for the Silivri M_w 5.7 mainshock, we perform a centroid moment tensor (CMT) inversion with a special focus on the reliability of non-DC components. We use the established ISOLated Asperities software package (Zahradník and Sokos, 2018) that was recently complemented by uncertainty analyses and validated on nonshear components of nuclear tests (Liu, Li, Zahradník, Sokos, Liu, and Tian, 2018; Liu, Li, Zahradník, Sokos, and Plicka, 2018). The seismic moment tensor (MT) is solved by the least-squares method, whereas the centroid position is grid searched. The uncertainty of MT and source depth is studied by utilizing covariance matrices (Hallo *et al.*, 2017; Vackář *et al.*, 2017). Multiple-point sources (MPS) are analyzed from regional seismic stations either with an iterative deconvolution or by a joint inversion with the nonnegative least-squares (NNLS) method (Zahradník and Sokos, 2014). Time shifts, artificially improving the fit between real and synthetic seismograms are not allowed. The MT is optionally retrieved as a full tensor, deviatoric, or DC constrained. Our waveform inversion is always accompanied by a detailed analysis of first-motion polarities (Liu and Zahradník, 2020).

In this study, centroids are grid searched beneath epicenters that are located by the probabilistic method NonLinLoc with station corrections (Lomax and Curtis, 2001), using the velocity model CRUST2.0, sampled at 40.9° N, 28.20° E (Bassin *et al.*, 2000). The mainshock was located at 40.8729° N, 28.2189° E, at 11 km depth, and the 24 September foreshock at 40.8729° N 28.2199° E at 10 km depth. The associated uncertainties are on the order of ±1 km horizontally and ±2 km vertically, respectively. For the regional CMT, we used waveform data from 16 broadband stations at 250–350 km epicentral distances (Fig. S1, available in the supplemental material to this article). The records were carefully selected, based on azimuthal coverage, signal-to-noise ratio, and data quality (in particular, avoiding instrumental disturbances, see Zahradník and Plešinger, 2010). Synthetic waveforms were calculated using the CRUST2.0 model. We also tested the velocity model of Karabulut *et al.* (2011), tailored specifically for the SoM, and obtained all major features of the solution including large negative CLVD value and its possible explanation with two DC subevents of different focal mechanisms as with CRUST2.0. Less extensive tests were also performed in the velocity models of Karabulut *et al.* (2021) and Novotný *et al.* (2001) and gave similar results.

Calibration Event

Because the present article is focused on non-DC components of the Silivri mainshock, it is essential to guarantee that these components are not false, produced by mismodeling in an inappropriate velocity model. The M_w 4.4 foreshock is well suited for this purpose. The full and deviatoric MT solution for this foreshock, assuming a single-point source model, is presented in Figure 2 and Table S1. The solution indicates a strike-slip-faulting mechanism with a minor thrust component. In the frequency band of 0.04–0.09 Hz, found as optimal by trial and error, the full MT solution fits the observed displacement seismograms with a variance reduction (VR) of 0.75; see Figure S2. It is characterized by a high DC component of ∼86% (CLVD ∼ −9% and isotropic component [ISO] ∼ +5%); for uncertainties obtained by the covariance-matrix approach, see histograms in Figure 2d. The low ISO component of the full MT is also confirmed by the deviatoric MT inversion, with VR = 0.75, and the corresponding histograms of DC and CLVD are similar. Both P and T axes are relatively well resolved (Fig. 2b). Furthermore, the dominant DC component and a stable focal mechanism

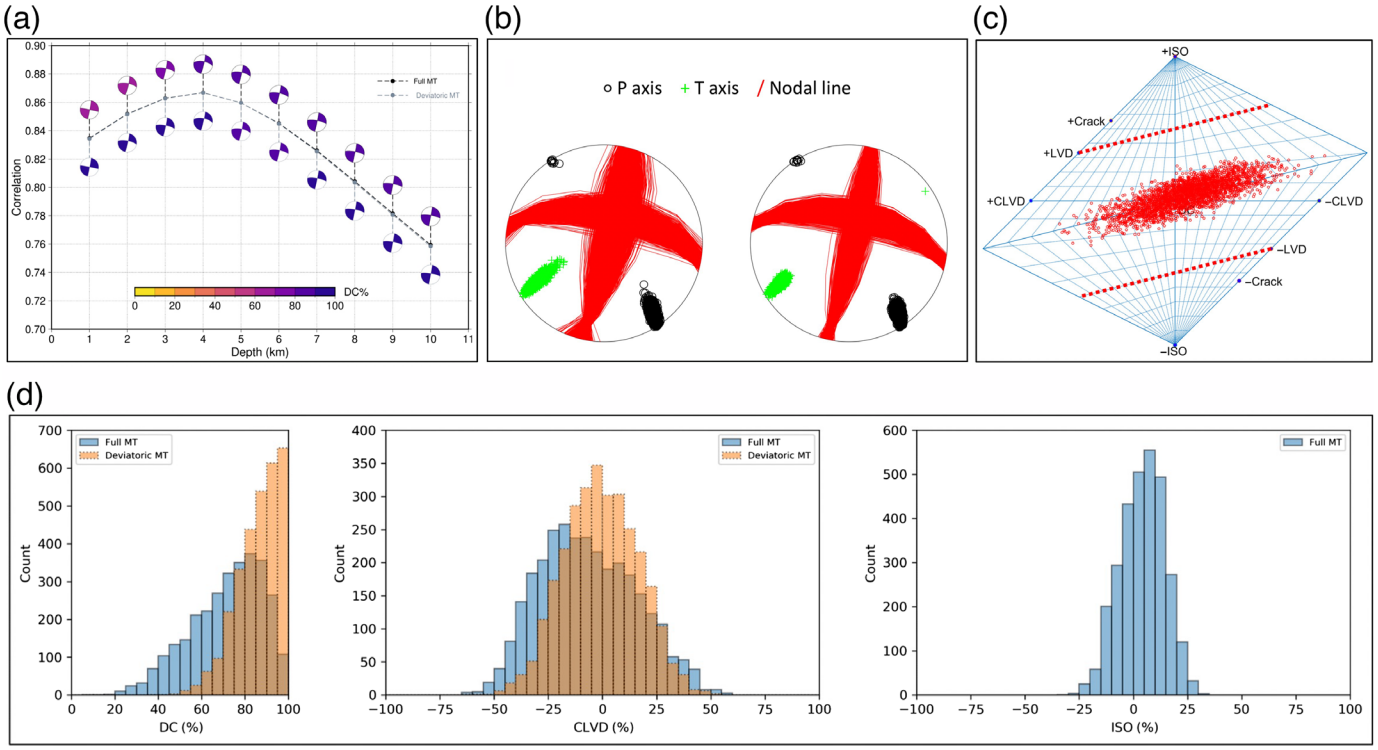

Figure 2. Full and deviatoric moment tensor (MT) solutions for a single-point source are presented in the frequency band of 0.04–0.09 Hz for the M_w 4.4 foreshock. (a) Correlation between observed and synthetic waveforms as a function of depth for both MT solutions. A high double-couple (DC) component is observed for each solution at all depths. (b) Uncertainties are shown by random sampling of the posterior probability density of model parameters. Consistent nodal lines (red solid line) and well-resolved P (black circle) and T axes (green plus sign) are retrieved. (c) The source-type plot (Hudson *et al.*, 1989) indicates a pure DC source for this event. (d) Histograms for DC, compensated linear vector dipole (CLVD), and isotropic component (ISO) components for full (blue with solid line border) and deviatoric MT (orange with dotted line border) solutions. The color version of this figure is available only in the electronic edition.

were confirmed by jackknife test, in which each time a single station was removed. The same strike/dip/rake angles and depth were also obtained in the DC-constrained inversion. Finally, we have checked the solution against 60 observed first-motion polarities; except for two (both close to nodal lines), all polarities matched the full, deviatoric, and DC-constrained MT models. Thus, we demonstrated that with the adopted velocity model, spurious departures from a standard DC source model are unlikely, and thus we can confidently attempt to resolve non-DC components of the mainshock.

Mainshock

To analyze the non-DC behavior of the 2019 Silivri mainshock, we again employed the CRUST2.0 model. In the frequency band of 0.03–0.06 Hz, the earthquake appears to be a point source; that is, in a multiple-point inversion, only one subevent is dominant. The full and deviatoric MT inversion provided similar results (Fig. 3). We obtained the centroid depth as 8 km (7–9 km) and a scalar moment of 3.9×10^{17} N · m. The waveform fit is satisfactory (VR = 0.73, Fig. S3). Both (full and deviatoric) focal mechanisms are similar to Global CMT (Fig. 1a), significantly deviating from a DC shear source. The best-fitting full MT is characterized by DC 41%, CLVD −54%, and ISO −5%. The uncertainties are shown in Figure 3b. Nodal lines of the DC part are more dispersed than in the calibration event, with a highly uncertain T axis, allowing for and indicating a variation from reverse to strike-slip faulting. Nevertheless, despite the uncertainties, three features are quite obvious: (1) the mainshock is not a pure DC event, (2) its CLVD component is significant and negative, and (3) its isotropic component is very low (if any). The result (3) explains why the full and deviatoric MT inversions give low DC% and large CLVD%, both resolving the same centroid depth of 8 km. The formally optimal strike/dip/rake angles (s/d/r; in °) are 259/31/117 (equivalent to 48/63/75).

For the mainshock, we analyzed 161 first-motion polarities from additional local and regional stations, and they strongly disagree with the full and deviatoric MT (Fig. 3e–g). Therefore, the question arises, whether the mainshock potentially included a subevent with shear DC faulting and, if so, what the faulting geometry might have been. To address this, we inverted the polarities into a DC model, using the FOCal MEChanism determinations code (Snoke, 2003). Almost all first-motion data (with just 1 misfit) can be explained by a strike-slip mechanism, characterized by strike/dip/rake angles

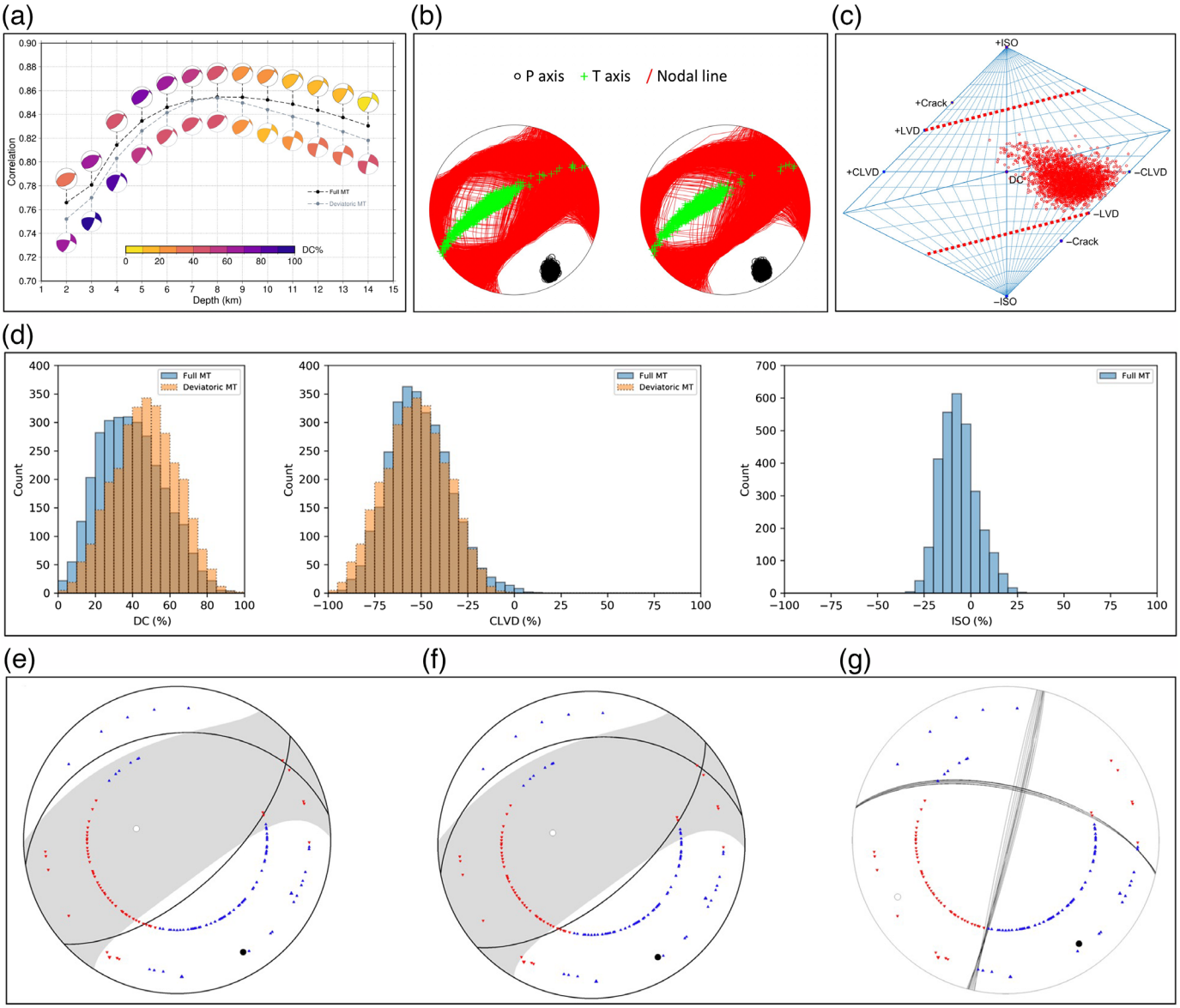

of 14/88/29 (283/61/178; Fig. 3g). This important observation undoubtedly suggested that the mainshock started with a shear (100% DC) faulting in strike-slip mode. Strike slip was also the foreshock's faulting type.

Interpretation of the CLVD Component

To resolve any source complexity in the mainshock, we extended the inverted frequency range; thus, the mainshock no longer appears to be a single point; two or more subevents of comparable moments may be needed to fit waveforms. In the frequency range of 0.03–0.08 Hz, we investigated one-, two-, and three-point MPS models. Relative to the one-subevent model, the two-subevent model improved the waveform fit (VR) by ~8%, whereas the improvement with the three-subevent model was weaker, and the third subevent was unstable. Thus, we focus on two-point models. In Figure 1b and Figure S4a, we present the two-point MPS results on a horizontal trial

Figure 3. Single-point-source approximation in the frequency band of 0.03–0.06 Hz for the M_w 5.7 mainshock. Full and deviatoric MT solutions are presented. (a) Correlation between observed and synthetic waveforms as a function of depth for both MT solutions. (b) Uncertainties are shown by random sampling of the posterior probability density of model parameters. (c) Source-type plot (Hudson *et al.*, 1989) highlighting the non-DC character of this earthquake. (d) Histograms for DC, compensated linear vector dipole (CLVD), and ISO components for full (blue with solid line border) and deviatoric MT (orange with dotted line border) solutions. (e–g) First-motion polarities (red inverted triangle for compression, blue triangle for dilatation) are compared with the waveform inversion for full MT (e), deviatoric MT (f), and with the FOCal MEChanism determinations (FOCMEC) solution (g). Shaded sectors refer to compression in calculated MTs, whereas nodal lines represent the double-couple part. Note the stable position of the P axis shown by the small filled black circle in the three focal mechanisms of panels (e–g). The color version of this figure is available only in the electronic edition.

source line with 1 km grid spacing, located at a depth of 8 km. The strike of the grid line is 290°, analogous to the strike of the aftershock sequence. By employing iterative deconvolution (Zahradník and Sokos, 2018), and seeking a DC-constrained mechanism, we detected a major subevent with a strike-slip mechanism, located close to the mainshock epicenter (1 km to the northwest). The second subevent with a thrust mechanism is located 6 km to the southeast, starting ∼1.5 s after the first one. The strike-slip (SS) subevent-1 is characterized by s/d/r angles of 17/88/30 (286/60/178) with a seismic moment of 2.68×10^{17} N · m (Table S1). The thrust-faulting (TF) subevent-2 is characterized by s/d/r angles of 104/73/106 (239/23/47) and a seismic moment of 1.04×10^{17} N · m. The moment ratio is TF/SS = 0.39, DC percentage of the tensor sum of two subevents is 58.9%. Note the spectacular similarity of subevent-1 to the strike-slip solution obtained from polarities. Thus, we acquire an independent indication that the earthquake started as a DC strike-slip but then continued as a thrust-faulting event, likely jumping onto an adjacent fault segment of a different orientation. Strictly speaking, although first-motion polarities prove a clearly 100% DC nature of the first subevent, and the total CLVD component of the earthquake can be explained with two DC subevents of different focal mechanisms, we cannot rule out that the second subevent might have included a nonshear faulting.

In case of two spatially close subevents, the performance of iterative deconvolution may not be optimal regarding the position and size of subevents; typically, the moment of subevent-1 may be overestimated relative to subevent-2 (Zahradník and Sokos, 2014). To this goal, we performed a joint search for SS–TF source pairs whose 100% DC focal mechanisms are fixed at the above s/d/r values. We systematically analyzed all possible source pairs on a linear grid, and jointly inverted waveforms for the position and moments of the pair members (the so-called NNLS technique described in the appendix of Zahradník and Sokos, 2014). Here, we again set the linear grid at the centroid depth (8 km), with 1 km spacing, azimuth 290°, and the total scalar moment of each subevent pair is constrained by the previous low-frequency CMT solution. As an example of the spatial and temporal stability of the solution, four best-fitting subevent pairs (VR > 0.65) are shown in Figure 1b and Figure S4b. The moment ratio TF/SS ∼0.5–0.6 is higher than in iterative deconvolution, as expected. Subevent-1 precedes subevent-2, in good agreement with the evidence from polarities. The best-fitting pair (VR = 0.66) indicates the strike-slip subevent-1 situated 1 km westward, and the thrust-fault subevent-2 at 4 km southeastward, relative to the epicenter. The summed moment tensors of the SS + TF pairs give CLVD of −52% to −59%, explaining the values obtained in the low-frequency CMT. Similar SS + TF two-point models were also obtained for trial source lines at other depths, for example, at the depth of 5 km. We also performed limited tests for a vertical trial plane (azimuth 290°) to check whether subevents 1 and 2 would prefer different depths, but the depth resolution was low due to relatively low inverted frequencies. Aftershocks relocation that we performed in different velocity models (but not reported here because the location problem is well covered by other published articles) did not indicate any systematic depth change along the 290° azimuth; thus, we stay in this article with subevents 1 and 2 at the same depth.

We conclude that the mainshock consisted of two episodes, starting as a strike slip and progressing as a thrust-faulting rupture, thus representing a closely spaced doublet with a mixed-type mechanism. The overall short duration of mainshock (2 s) has been also reported by SCARDEC (Vallée and Douet, 2016; see Data and Resources). This remarkable multifaulting behavior may have a causal relation with two other observations: The source mechanism of the foreshock M_w 4.4, collocated with the mainshock, was strike-slip faulting, whereas the eastward shifted aftershocks M_w 4.0 and 4.4 of September 2019 and January 2020 aftershocks exhibited thrust faulting (Fig. 1a).

Discussion

In earthquake source mechanism studies, an observed deviation from shear faulting, that is, a non-DC mechanism is evidence of a complex fault system unless spuriously imposed (Frohlich, 1995). Deciphering coseismic rupture evolution of large earthquakes in space and time along continental transform faults is relatively straightforward because rupture complexity can be verified by geological and geodetic studies. The significant deviation from pure shear faulting observed in the M_s 6.8 Armenian earthquake was explained by four DC subevents of strike-slip and dip-slip faulting (using the waveform inversion of long-period and broadband data) was also supported by field observations (Pacheco *et al.*, 1989; Kikuchi *et al.*, 1993). The 2017 M_w 7.8 Kaikōura, New Zealand, earthquake occurred at the termination of a subduction margin and a transform fault inducing a strong non-DC component (Cesca *et al.*, 2017). Multiple-source inversion of the MT for this event allowed identification of three distinct DC episodes: strike-slip-, oblique-, and thrust faulting reflecting the fault complexity in the region, which can be verified by the field observations (Duputel and Rivera, 2017). Resolving complex rupture evolution of moderate-size sources is more compelling especially if the faults are buried or submerged. Nevertheless, the decomposition of MT elucidated that the 2018 M_w 5.6 Osaka earthquake included strike-slip and reverse-faulting episodes in accordance with the observed aftershocks (Hallo *et al.*, 2019). Similarly, Global CMT reported that the CLVD component of the 2019 M_w 5.7 Changning earthquake was −98%, later deciphered as two DC subevents (Liu and Zahradník, 2020). The significant CLVD component observed for the 2019 M_w 5.7 Silivri earthquake similarly reflects the complexity of the MMF, comprising fault segmentation and bending (Le Pichon *et al.*, 2001; Armijo *et al.*, 2002; Laigle *et al.*, 2008).

In this study, we demonstrate that the Silivri mainshock consisted of two distinct subevents (fault segments of different orientation) by analyzing non-DC mechanisms, inverting waveforms into multiple DC point models, and incorporating a first-motion polarity analysis. The first subevent was identified as a strike-slip mechanism in agreement with the general right-lateral strike-slip character of the MMF. The east–west-trending strike of the MMF continues as the southern boundary of the central basin below the SoM. The Silivri earthquake occurred at the eastern tip of this basin, off the MMF, and likely on a subparallel, secondary fault, on a north dipping plane of 55°–60° (Durand *et al.*, 2020; Yamamoto *et al.*, 2020; Karabulut *et al.*, 2021).

The second subevent of the Silivri mainshock we identified is characterized by a thrust-faulting mechanism. Most likely, a subsidiary thrust fault located ~5 km to the east of the epicenter was activated. Interruption of a strike-slip movement by a restraining bend results in transpression, associated with crustal shortening. Examples are the Carboneras fault (Keller *et al.*, 1995) or the Dead Sea fault system (Gomez *et al.*, 2007; Nabavi *et al.*, 2017). Because of the local geometry of bending or side-stepping of en echelon faults, zones of subsidence or uplift formed along with the MMF. At the eastern tip of the Central Basin, along the western boundary of the Central High, the geometry of the MMF is reflected as shortening where the Silivri earthquake sequence is situated. The stress field of this particular region indicates transpression or thrust faulting due to uplift areas (see fig. 5 of Hergert and Heidbach, 2011). Generally, the central part of MMF is considered an almost vertical strike-slip fault, but the transition between the Central Basin and the Central High has been interpreted as a system of steeply dipping thrust and oblique-throw-compressional faults (Le Pichon *et al.*, 2001; Şengör *et al.*, 2014). This is also demonstrated in shear-box experiments that strike-slip faults are often associated with en-échelon arrangements and thrust faults form perpendicular to the shortening axis, at an angle of 45° to the principal deformation zone (Tchalenko, 1970; Sylvester, 1988). Therefore, our finding of the notable constituent of the mainshock represented by a thrust-fault segment (subevent-2) is geologically feasible. Choosing between the conjugated solutions characterized by s/d/r 104/73/106 (239/23/47), the strike of 239° is more likely with a northwest-dipping plane. Our observation supports the argument that the Silivri seismic sequence occurred within the shear zone of MMF on secondary faults (Karabulut *et al.*, 2021). Because of the limited depth resolution of subevents 1 and 2 of our two-segment model (SS + TF), we cannot rule out a possibility that the secondary shallower thrust structures could exist on top of the Main Marmara strike-slip fault.

Two previous earthquake source studies regarding the Silivri mainshock are comparable to this study. A recent study, Karabulut *et al.* (2021), assuming a point source model, inverted for moment tensor utilizing a DC-constrained Cut and Paste Method and fit the complex process with a single-fault strike-slip model because the second (thrust fault) subevent is smaller. It is analogous to Sokos *et al.* (2020) who also could model the complex Zakynthos earthquake relatively well with a single fault although the two-fault approximation was better. Employing teleseismic and regional waveforms, Irmak *et al.* (2021) obtained a full (non-DC) moment tensor similar to Global CMT and also similar to our result (Fig. 3). The DC part of the solution by Irmak *et al.* (2021) is a thrust fault, differing from the strike-slip faulting proposed by Karabulut *et al.* (2021). An explanation for this ambiguity can be found in our uncertainty analysis (Fig. 3b) in which the P axis is significantly better resolved than the T axis, as shown in Figure 3e–g; the thrust and strike-slip faulting have nearly the same P axis and differ only in the T axis. Karabulut *et al.* (2021) calculated slip distribution on a single fault plane (strike/dip/rake = 281°/60°/165°) employing eight stations at distances 30–100 km, whereas we calculated two-point source models from 16 stations at distances 250–350 km and lower frequencies. Despite these differences, the major slip patch of Karabulut *et al.* (2021) has an analogous position and strike-slip faulting similar to the first (early) major subevent of our solution. The slip inversion of Irmak *et al.* (2021) indicates a similar major slip patch as Karabulut *et al.* (2021) and our study, although it is a thrust faulting (strike/dip/rake = 271°/33°/110°), not strike slip; mainly because their fault plane strike angles were similar, 271° and 281°. However, because the fault plane of Irmak *et al.* (2021) had different dip and rake angles than Karabulut *et al.* (2021), and because Irmak *et al.* (2021) used 31 stations, they were able to interpret a delayed thrust-fault subevent situated eastward of the main patch as a stable feature. This feature is analogous to the second subevent of our two-fault model. Moreover, Karabulut *et al.* (2021) emphasized the increased reverse faulting components of aftershock focal mechanisms in the eastern part of the activated zone, in agreement with our observations.

In the light of these arguments, all three studies are complementary. Our uncertainty analysis of full MT provided trustful evidence of a large negative CLVD, which indicated source complexity. Multiple-point modeling was flexible enough to identify two episodes with different faulting styles. Slip inversions in the other studies were robust enough to reveal the almost identical position of the major slip area (although in one it was strike slip, whereas in the other it was reverse mechanism). However—due to the single-fault plane assumption—their approach could not reveal two subsequent episodes of different faulting styles during the mainshock.

The ongoing concern about a future strong earthquake on the MMF is whether it will rupture as a thoroughgoing single segment or consecutively activate multiple segments. A more challenging question is whether the rupture will employ

secondary (and/or blind) faults within the shear zone (Géli *et al.*, 2021). In light of our observations, the expected major earthquake may not be a single rupture with a single focal mechanism within the shear zone of MMF. Instead, it may also involve dip-slip faulting together with strike slip; especially if the nucleation point is in the proximity of fault bends or jogs.

Regarding the dip-slip mechanisms and tsunamis, Altınok *et al.* (2011) listed four tsunamis affecting the SoM coast in the 20th century. With more than 15 million inhabitants, the megacity Istanbul and the entire Marmara region host key infrastructure and main industrial facilities fueling the Turkish economy. The infrastructures for gas, electricity, shipyards, and industrial facilities located along the shoreline are exposed to significant tsunami hazards (Hancilar *et al.*, 2012). The tsunami generated in the 1999 M_w 7.4 İzmit earthquake can only be explained with the addition of dip-slip faults (Tinti *et al.*, 2006). This conclusion should impact the physically based future versions of the seismic hazard (and risk) reassessment of the region, and should also be considered in the development of next generation early warning systems.

Conclusion

The central segment of the Main Marmara fault (MMF) below the Sea of Marmara acts as a seismic gap and is expected to host a major earthquake in the near future. The 2019 M_w 5.7 Silivri earthquake provided a unique opportunity to estimate how a future event may look like in terms of coseismic rupture evolution. The Silivri earthquake occurred at the eastern tip of central basin where southern and northern boundary faults merge, clearly demonstrating the susceptibility of the region to mixed-type seismic faulting as reported in this study. The 10-day long seismic sequence activated an ~8–km-long and 3–km-wide zone, almost map-view parallel to the MMF. The M_w 4.4 foreshock, located at the western end of the mainhock rupture, had a strike-slip mechanism, whereas several M_w 4-size aftershocks to the east were thrust mechanisms. We here resolve this puzzle by reporting that the mainshock integrated both features. The source process is modeled by inverting the near regional waveforms for multiple subevents allowing to decipher that the Silivri mainshock nucleated as strike-slip faulting, almost coincidentally with the foreshock position, and progressed by rupturing a thrust-faulting eastern segment. The mainshock as a whole was a relatively compact doublet, closely spaced both in space (5–7 km) and time (<2 s). The seismic evidence of the thrust-faulting episode of the mainshock can be explained as activation of the geologically anticipated subsidiary faulting in the uplift transpression region related to crustal shortening at the eastern tip of the Central Basin, along the western boundary of the Central High. Accordingly, the expected future major earthquake within this shear zone may not have a simple faulting mechanism. Besides other implications, it means that the tsunamigenic potential of MMF during a future major earthquake should be considered. The possible length of such critical submerged fault segments of varying orientations needs to be studied by near-fault seismic stations involving permanent Ocean Bottom Seismograph deployments in the region.

Data and Resources

Regional waveform data used in this study were obtained from Kandilli Observatory and Earthquake Research Institute (KOERI—KO), available at https://eida.koeri.boun.edu.tr (last accessed July 2022), Disaster and Emergency Management Presidency of Turkey (AFAD—TU), available at https://tdvms.afad.gov.tr (last accessed July 2022), National Observatory of Athens (NOA—HL) and Aristotle University of Thessaloniki (AUTH—HT), available at https://eida.gein.noa.gr (last accessed July 2022), and from National Seismic Network of Bulgaria (BS), available at http:/eida-sc3.infp.ro/fdsnws (last accessed July 2022). ISOLated Asperities-graphical user interface (ISOLA-GUI) software can be downloaded from http://geo.mff.cuni.cz/~jz/for_ISOLAnews/ (last accessed July 2022). FOCal MEChanism determinations (FOCMEC) software can be downloaded from http://www.iris.edu/pub/programs/focmec/ (last accessed March 2022). NonLinLocv7.00 software was used and can be downloaded from http://alomax.free.fr/nlloc/ (last accessed July 2022). The maps were generated using the Generic Mapping Tools v.5.4.3 (Wessel and Smith, 1991) and can be downloaded from https://www.generic-mapping-tools.org/ (last accessed July 2022). ObsPy (Beyreuther *et al.*, 2010) and Pyrocko (Heimann *et al.*, 2017) were used for data processing. In the supplemental material, we provide one table and four additional figures to better illustrate the findings presented in the main text. The other relevant data to this article were available at http://scardec.projects.sismo.ipgp.fr (last accessed March 2022).

Declaration of Competing Interests

The authors acknowledge that there are no conflicts of interest recorded.

Acknowledgments

Constructive comments of Editor Allison Bent, Reviewer C. Evangelidis, and two anonymous reviewers improved the article. D. A. would like to thank Anthony Lomax for his support in employing the NonLinLocv7.00 software.

References

Altınok, Y., B. Alpar, N. Ozer, and H. Aykurt (2011). Revision of the tsunami catalogue affecting Turkish coasts and surrounding regions, *Nat. Hazards Earth Syst. Sci.* **11,** 273–291.

Ambraseys, N. N., and J. A. Jackson (2000). Seismicity of the Sea of Marmara (Turkey) since 1500, *Geophys. J. Int.* **141,** no. 3, F1–F6.

Armijo, R., B. Meyer, S. Navarro, G. King, and A. Barka (2002). Asymmetric slip partitioning in the Sea of Marmara pull-apart: A clue to propagation processes of the North Anatolian fault? *Terra Nova* **14,** 80–86.

Barka, A. (1992). The North Anatolian fault zone, *Annales Tectonicae* **6,** 164–195.

Bassin, C., G. Laske, and G. Masters (2000). The current limits of resolution for surface wave tomography in North America, *Eos Trans. AGU* **81,** F897.

Bécel, A., M. Laigle, B. de Voogd, A. Hirn, T. Taymaz, S. Yolsal-Cevikbilen, and H. Shimamura (2010). North Marmara trough architecture of basin infill, basement and faults, from PSDM reflection and OBS refraction seismic, *Tectonophysics* **490,** nos. 1/2, 1–4, doi: 10.1016/j.tecto.2010.04.004.

Beyreuther, M., R. Barsch, L. Krischer, T. Megies, Y. Behr, and J. Wassermann (2010). ObsPy: A Python toolbox for seismology, *Seismol. Res. Lett.* **81,** no. 3, 530–533, doi: 10.1785/gssrl.81.3.530.

Bohnhoff, M., F. Bulut, G. Dresen, P. E. Malin, T. Eken, and M. Aktar (2013). An earthquake gap south of Istanbul, *Nat. Commun.* **18,** no. 4, 1–6, doi: 10.1038/ncomms2999.

Bohnhoff, M., P. Martinez-Garzon, F. Bulut, and Y. Ben-Zion (2016). Maximum earthquake magnitudes along different sections of the North Anatolian fault zone, *Tectonophysics* **674,** 147–165.

Bohnhoff, M., C. Wollin, D. Domigall, L. Küperkoch, P. Martínez-Garzón, G. Kwiatek, G. Dresen, and P. E. Malin (2017). Repeating Marmara Sea earthquakes: Indication for fault creep, *Geophys. J. Int.* **210,** no. 1, 332–339, doi: 10.1093/gji/ggx169.

Cesca, C., Y. Zhang, V. Mouslopoulou, R. Wang, J. Saul, M. Savage, and S. Heimann (2017). Complex rupture process of the Mw 7.8, 2016, Kaikoura earthquake, New Zealand, and its aftershock sequence, *Earth Planet. Sci. Lett.* **478,** 110–120, doi: 10.1016/j.epsl.2017.08.024.

Cesca, S., J. Letort, H. N. Razafindrakoto, S. Heimann, E. Rivalta, M. P. Isken, M. Nikkhoo, L. Passarelli, G. M. Petersen, F. Cotton, *et al.* (2020). Drainage of a deep magma reservoir near Mayotte inferred from seismicity and deformation, *Nature Geosci.* **13,** 87–93, doi: 10.1038/s41561-019-0505-5.

Demirbağ, E., C. Rangin, X. Le Pichon, and C. Şengör (2003). Investigation of the tectonics of the Main Marmara fault, by means of deep-towed seismic data, *Tectonophysics* **361,** 1–19, doi: 10.1016/S0040-1951(02)00535-8.

Duputel, Z., and L. Rivera (2017). Long-period analysis of the 2016 Kaikoura earthquake, *Phys. Earth Planet. In.* **265,** 62–66, doi: 10.1016/j.pepi.2017.02.004.

Durand, V., S. Bentz, G. Kwiatek, G. Dresen, C. Wollin, O. Heidbach, P. Martínez-Garzón, F. Cotton, M. Nurlu, and M. Bohnhoff (2020). A two-scale preparation phase preceded an M_w 5.8 earthquake in the Sea of Marmara offshore Istanbul, Turkey, *Seismol. Res. Lett.* doi: 10.1785/0220200110.

Dziewonski, A. M., T. A. Chou, and J. H. Woodhouse (1981). Determination of earthquake source parameters from waveform data for studies of global and regional seismicity, *J. Geophys. Res.* **86,** 2825–2852, doi: 10.1029/JB086iB04p02825.

Ekström, G., M. Nettles, and A. M. Dziewonski (2012). The global CMT project 2004-2010: Centroid-moment tensors for 13,017 earthquakes, *Phys. Earth Planet. In.* **200–201,** doi: 10.1016/j.pepi.2012.04.002.

Ergintav, S., R. E. Reilinger, R. Çakmak, M. Floyd, Z. Cakir, U. Doğan, R. W. King, S. McClusky, and H. Özener (2014). Istanbul's earthquake hot spots: Geodetic constraints on strain accumulation along faults in the Marmara seismic gap, *Geophys. Res. Lett.* **41,** no. 16, 5783–5788, doi: 10.1002/2014gl060985.

Frohlich, C. (1995). Characteristics of well-determined non-double-couple earthquakes in the Harvard CMT catalog, *Phys. Earth Planet. In.* **91,** 213–228.

Gasperini, L., M. Stucchi, V. Cedro, M. Meghraoui, G. Ucarkus, and A. Polonia (2021). Active fault segments along the North Anatolian fault system in the Sea of Marmara: Implication for seismic hazard, *Med. Geosci. Rev.* **3,** no. 1, 29–44, doi: 10.1007/s42990-021-00048-7.

Géli, L., P. Henry, and N. Cagatay (2021). A review of 20 years (1999–2019) of Turkish–French collaboration in marine geoscience research in the Sea of Marmara, *Med. Geosci. Rev.* **3,** 3–27, doi: 10.1007/s42990-021-00055-8.

Gomez, F., T. Nemer, C. Tabet, M. Khawlie, M. Meghraoui, and M. Barazangi (2007). Strain partitioning of active transpression within the Lebanese Restraining Bend of the Dead Sea fault (Lebanon and SW Syria), in *Tectonics of Strike-Slip Restraining and Releasing Bends in Continental and Oceanic Settings*, D. Cunningham and P. Mann (Editors), Geological Society of London Special Publication, London, United Kingdom.

Hallo, M., K. Asano, and F. Gallovič (2017). Bayesian inference and interpretation of centroid moment tensors of the 2016 Kumamoto earthquake sequence, Kyushu, Japan, *Earth Planets Space* **69,** 1–9, doi: 10.1186/s40623-017-0721-4.

Hallo, M., I. Opršal, K. Asano, and F. Gallovič (2019). Seismotectonics of the 2018 northern Osaka M6.1 earthquake and its aftershocks: Joint movements on strike-slip and reverse faults in inland Japan, *Earth Planets Space* **71,** 1–21, doi: 10.1186/s40623-019-1016-8.

Hancilar, U., E. Çaktı, and M. Erdik (2012). Earthquake performance assessment and rehabilitation of two historical unreinforced masonry buildings, *Bull. Earthq. Eng.* **10,** 307–330, doi: 10.1007/s10518-011-9281-3.

Heimann, S., M. Kriegerowski, M. Isken, S. Cesca, S. Daout, F. Grigoli, C. Juretzek, T. Megies, N. Nooshiri, A. Steinberg, *et al.* (2017). Pyrocko—An open-source seismology toolbox and library V. 0.3, *GFZ Data Services*, doi: 10.5880/GFZ.2.1.2017.001.

Hergert, T., and O. Heidbach (2011). Geomechanical model of the Marmara Sea region—II. 3-D contemporary background stress field, *Geophys. J. Int.* **185,** no. 3, 1090–1102, doi: 10.1111/j.1365-246X.2011.04992.x.

Hrubcová, P., J. Doubravová, and V. Vavryčuk (2021). Non-double-couple earthquakes in 2017 swarm in Reykjanes peninsula, SW Iceland: Sensitive indicator of volcano-tectonic movements at slow-spreading rift, *Earth Planet. Sci. Lett.* **563,** doi: 10.1016/j.epsl.2021.116875.

Hudson, J. A., R. G. Pearce, and R. M. Rogers (1989). Source type plot for inversion of the moment tensor, *J. Geophys. Res.* **94,** no. B1, 765–774.

Imren, C., X. Le Pichon, C. Rangin, E. Demirbağ, B. Ecevitoğlu, and N. Görür (2001). The North Anatolian fault within the Sea of Marmara: A new interpretation based on multichannel seismic and multi-beam bathymetry data, *Earth Planet. Sci. Lett.* **186,** 143–158.

Irmak, T. H., S. Yolsal-Çevikbilen, T. Eken, B. Doğan, C. Erman, and E. Yavuz (2021). Source characteristics and seismotectonic implications of the 26 September 2019 *Mw* 5.7 Silivri High-Kumburgaz basin earthquake and evaluation of its aftershocks at the North Anatolian fault zone (central Marmara Sea, NW Turkey), *Geophys. J. Int.* **227,** no. 1, 383–402, doi: 10.1093/gji/ggab233.

Julia, J., A. A. Nyblade, R. Durrheim, L. Linzer, R. Gök, P. Dirks, and W. Walter (2009). Source mechanisms of mine-related seismicity, Savuka Mine, South Africa, *Bull. Seismol. Soc. Am.* **99,** no. 5, 2801–2814, doi: 10.1785/0120080334.

Julian, B. R., A. D. Miller, and G. R. Foulger (1998). Non-double couple earthquakes, *Rev. Geophys.* **36,** no. 4, 525–549.

Karabulut, H., S. E. Güvercin, F. Eskiköy, A. Ö. Konca, and S. Ergintav (2021). The moderate size 2019 September M w 5.8 Silivri earthquake unveils the complexity of the Main Marmara fault shear zone, *Geophys. J. Int.* **224,** no. 1, 377–388.

Karabulut, H., J. Schmittbuhl, S. Özalaybey, O. Lengliné, A. Kömeç-Mutlu, V. Durand, M. Bouchon, G. Daniel, and M. P. Bouin (2011). Evolution of the seismicity in the eastern Marmara Sea a decade before and after the 17 August 1999 Izmit earthquake, *Tectonophysics* **510,** 17–27, doi: 10.1016/j.tecto.2011.07.009.

Keller, J. V. A., S. H. Hall, C. J. Dart, and K. R. McClay (1995). The geometry and evolution of a transpressional strike-slip system: The Carboneras fault, SE Spain, *J. Geol. Soc.* **152,** 339–351, doi: 10.1144/gsjgs.152.2.0339.

Kikuchi, M., H. Kanamori, and K. Satake (1993). Source complexity of the 1988 Armenian earthquake: Evidence for a slow after-slip event, *J. Geophys. Res.* **98,** no. B9, 15,797–15,808.

Laigle, M., A. Bécel, B. de Voogd, A. Hirn, T. Taymaz, and S. Ozalaybey (2008). A first deep seismic survey in the Sea of Marmara: Deep basins and whole crust architecture and evolution, *Earth Planet. Sci. Lett.* **270,** 168–179, doi: 10.1016/j.epsl.2008.02.031.

Lange, D., H. Kopp, J. Y. Royer, P. Henry, Z. Çakir, F. Petersen, P. Sakic, V. Ballu, J. Bialas, M. Özeren, *et al.* (2019). Interseismic strain build-up on the submarine North Anatolian fault offshore Istanbul, *Nat. Commun.* **10,** 1–9, doi: 10.1038/s41467-019-11016-z.

Lay, T., Z. Duputel, L. Ye, and H. Kanamori (2013). The December 7, 2012 Japan trench intraplate doublet (M_w 7.2, 7.1) and interactions between near-trench intraplate thrust and normal faulting, *Phys. Earth Planet. In.* **220,** 73–78, doi: 10.1016/j.pepi.2013.04.009.

Le Pichon, X., A. M. C. Sengor, E. Demirbag, C. Rangin, C. Imren, R. Armijo, N. Gorur, N. Cagatay, B. M. de Lepiney, and B. Meyer (2001). The active main Marmara fault, *Earth Planet. Sci. Lett.* **192,** no. 4, 595–616, doi: 10.1016/S0012-821X(01)00449-6.

Liu, J., and J. Zahradník (2020). The 2019 M_w 5.7 Changning earthquake, Sichuan basin, China: A shallow doublet with different faulting styles, *Geophys. Res. Lett.* **47,** e2019GL085408, doi: 10.1029/2019GL085408.

Liu, J., L. Li, J. Zahradník, E. Sokos, C. Liu, and X. Tian (2018). North Korea's 2017 test and its non-tectonic aftershock, *Geophys. Res. Lett.* **45,** 3017–3025, doi: 10.1002/2018GL077095.

Liu, J., L. Li, J. Zahradník, E. Sokos, and V. Plicka (2018). Generalized source model of the North Korea tests 2009–2017, *Seismol. Res. Lett.* **89,** no. 6, 2166–2173, doi: 10.1785/0220180106.

Lomax, A., and A. Curtis (2001). Fast, probabilistic earthquake location in 3D models using oct-tree importance sampling, *Geophys. Res. Abstr.* **3,** no. 955, 10–1007.

Martínez-Garzón, P., G. Kwiatek, M. Bohnhoff, and G. Dresen (2017). Volumetric components in the earthquake source related to fluid injection and stress state, *Geophys. Res. Lett.* **44,** no. 2, 800–809, doi: 10.1002/2016GL071963.

Miller, A. D., B. R. Julian, and G. R. Foulger (1998). Three-dimensional seismic structure and moment tensors of non-double-couple earthquakes at the Hengill-Grensdalur volcanic complex, Iceland, *Geophys. J. Int.* **133,** 309–325.

Nabavi, S. T., S. A. Alavi, S. Mohammadi, and M. R. Ghassemi (2017). Mechanical evolution of transpression zones affected by fault interactions: Insights from 3D elasto-plastic finite element models, *J. Struct. Geol.* **106,** 19–40, doi: 10.1016/j.jsg.2017.11.003.

Novotný, O., J. Zahradník, and G.-A. Tselentis (2001). Northwestern Turkey earthquakes and the crustal structure inferred from surface waves observed in western Greece, *Bull. Seismol. Soc. Am.* **91,** no. 4, 875–879, doi: 10.1785/0120000116.

Okay, A., A. Kaslılar-Özcan, C. Imren, A. Boztepe-Güney, E. Demirbag, and I. Kusçu (2000). Active faults and evolving strike-slip basins in the Marmara Sea, northwest Turkey: A multichannel seismic reflection study, *Tectonophysics* **321,** 189–218, doi: 10.1016/S0040-1951(00)00046-9.

Örgülü, G. (2011). Seismicity and source parameters for small-scale earthquakes along the splays of the North Anatolian fault (NAF) in the Marmara Sea, *Geophys. J. Int.* **184,** no. 1, 385–404, doi: 10.1111/j.1365-246X.2010.04844.x.

Pacheco, J. F., C. H. Estabrook, D. W. Simpson, and J. L. Nabelek (1989). Teleseismic body wave analysis of the 1988 Armenian earthquake, *Geophys. Res. Lett.* **16,** no. 12, 1425–1428.

Parke, J. R., R. S. White, D. McKenzie, T. A. Minshull, J. M. Bull, I. Kuscu, N. Görür, and A. M. C. Şengör (2002). Interaction between faulting and sedimentation in the Sea of Marmara, western Turkey, *J. Geophys. Res.* **107,** doi: 10.1029/2001JB000450.

Parsons, T. (2004). Recalculated probability of M ≥ 7 earthquakes beneath the Sea of Marmara, Turkey, *J. Geophys. Res.* **109,** no. B5, doi: 10.1029/2003jb002667.

Rangin, C., X. Le Pichon, E. Demirbağ, and C. Imren (2004). Strain localization in the Sea of Marmara: Propagation of the North Anatolian fault in a now inactive pull-apart, *Tectonics* **13,** TC2014 , doi: 10.1029/2002TC001437.

Reilinger, R., S. McClusky, P. Vernant, S. Lawrence, S. Ergintav, R. Cakmak, and H. Ozener (2006). GPS constraints on continental deformation in the Africa-Arabia-Eurasia continental collision zone and implications for the dynamics of plate interactions, *J. Geophys. Res.* **111,** no. B5, doi: 10.1029/2005JB004051.

Sato, T., J. Kasahara, T. Taymaz, M. Ito, A. Kamimura, T. Hayakawa, and O. Tan (2004). A study of microearthquake seismicity and focal mechanisms within the Sea of Marmara (NW Turkey) using ocean-bottom seismometers (OBSs), *Tectonophysics* 391**,** 303–314.

Schmittbuhl, J., H. Karabulut, O. Lengliné, and M. Bouchon (2016). Seismicity distribution and locking depth along the Main Marmara fault, Turkey, *Geochem. Geophys. Geosys.* **17,** 954–965, doi: 10.1002/2015GC006120.

Şengör, A. M. C., C. Grall, C. Imren, X. Le Pichon, N. Ambraseys, P. Henry, H. Karabulut, and M. Siyako (2014). The geometry of the North Anatolian transform fault in the Sea of Marmara and its temporal evolution: Implications for the development of intracontinental transform faults, *Can. J. Earth Sci.* **51,** no. 3, 222–242.

Şengör, A. M. C., O. Tüysüz, C. İmren, M. Sakınç, H. Eyidoğan, N. Görür, X. Le Pichon, and C. Rangin (2005). The North Anatolian fault: A new look, *Annu. Rev. Earth Planet. Sci.* **33,** 37–112.

Shuler, A., G. Ekström, and M. Nettles (2013). Physical mechanisms for vertical CLVD earthquakes at active volcanoes, *J. Geophys. Res.* **118,** 1569–1586, doi: 10.1002/jgrb.50131.

Šílený, J., and A. Milev (2006). Seismic moment tensor resolution on a local scale: Simulated rockburst and mine-induced seismic events in the Kopanang Gold Mine, South Africa, *Pure Appl. Geophys.* **163,** 1495–1513, doi: 10.1007/s00024-006-0089-z.

Sipkin, S. (1986). Interpretation of non-double couple earthquake mechanisms derived from moment tensor inversion, *J. Geophys. Res.* **91,** no. B1, 531–547.

Snoke, J. A. (2003). FOCMEC: FOCal MEChanism determinations, in *International Handbook of Earthquake and Engineering Seismology*, W. H. K. Lee, H. Kanamori, P. C. Jennings, and C. Kisslinger (Editors), Academic Press, Amsterdam, 1629–1630.

Sokos, E., F. Gallovič, C. P. Evangelidis, A. Serpetsidaki, V. Plicka, J. Kostelecký, and J. Zahradník (2020). The 2018 Mw 6.8 Zakynthos, Greece, earthquake: Dominant strike-slip faulting near subducting slab, *Seismol. Res. Lett.* doi: 10.1785/0220190169.

Sylvester, A. G. (1988). Strike-slip faults, *Geol. Soc. Am. Bull.* **100,** 1666–1703.

Tchalenko, J. S. (1970). Similarities between shear zones of different magnitudes, *Geol. Soc. Am. Bull.* **81,** 1625–1640.

Tinti, S., A. Armigliato, A. Manucci, G. Pagnoni, F. Zaniboni, A. C. Yalciner, and Y. Altinok (2006). The generating mechanisms of the August 17, 1999 Izmit bay (Turkey) tsunami: Regional (tectonic) and local (mass instabilities) causes, *Mar. Geol.* **225,** 311–330.

Vackář, J., F. Gallovič, J. Burjánek, J. Zahradník, and J. Clinton (2017). Bayesian ISOLA: New tool for automated centroid moment tensor inversion, *Geophys. J. Int.* **210,** 693–705, doi: 10.1093/gji/ggx158.

Vallée, M., and V. Douet (2016). A new database of source time functions (STFs) extracted from the SCARDEC method, *Phys. Earth Planet. In.* **257,** 149–157, doi: 10.1016/j.pepi.2016.05.012.

Wessel, P., and W. F. H. Smith (1991). Free software helps map and display data, *Eos. Trans. AGU* **72,** 441–446, doi: 10.1029/90EO00319.

Wollin, C., M. Bohnhoff, P. Martínez-Garzón, L. Küperkoch, and C. Raub (2018). A unified earthquake catalogue for the Sea of Marmara region, Turkey, based on automatized phase picking and travel-time inversion: Seismotectonic implications, *Tectonophysics* **747,** 416–444, doi: 10.1016/j.tecto.2018.05.020.

Wollin, S., M. Bohnhoff, V. Vavrycuk, and P. Martinez-Garzon, (2019). Stress inversion of regional seismicity in the Sea of Marmara region, Turkey, *Pure Appl. Geophys.* doi: 10.1007/s00024-018-1971-1.

Wong, H. K., T. Lüdmann, A. Uluğ, and N. Görür (1995). The Sea of Marmara: A boundary sea in an escape tectonic regime, *Tectonophysics* **244,** 231–250, doi: 10.1016/0040-1951(94)00245-5.

Yamamoto, R., M. Kido, Y. Ohta, N. Takahashi, Y. Yamamoto, A. Pinar, D. Kalafat, D. H. Ozener, and Y. Kaneda (2019). Seafloor geodesy revealed partial creep of the North Anatolian fault submerged in the Sea of Marmara, *Geophys. Res. Lett.* **46,** no. 3, 1268–1275, doi: 10.1029/2018GL080984.

Yamamoto, Y., D. Kalafat, A. Pinar, N. Takahashi, Z. Coskun, R. Polat, Y. Kaneda, and H. Ozener (2020). Fault geometry beneath the western and central Marmara Sea, Turkey, based on ocean bottom seismographic observations: Implications for future large earthquakes, *Tectonophysics* **791,** doi: 10.1016/j.tecto.2020.228568.

Yamamoto, Y., N. Takahasi, A. Pinar, D. Kalafat, S. Citak, M. Comoglu, R. Polat, and Y. Kaneda (2017). Geometry and segmentation of the North Anatolian fault beneath the Marmara Sea, Turkey, deduced from long-term ocean bottom seismographic observations, *J. Geophys. Res.* **122,** doi: 10.1002/2016JB013608.

Zahradník, J., and A. Plešinger (2010). Toward understanding subtle instrumentation effects associated with weak seismic events in the near field, *Bull. Seismol. Soc. Am.* **100,** no. 1, 59–73, doi: 10.1785/0120090087.

Zahradník, J., and E. Sokos (2014). The Mw 7.1 Van, eastern Turkey, earthquake 2011: Two-point source modelling by iterative deconvolution and non-negative least squares, *Geophys. J. Int.* **196,** no. 1, 522–538, doi: 10.1093/gji/ggt386.

Zahradník, J., and E. Sokos (2018). ISOLA code for multiple-point source modeling—Review, in *Moment Tensor Solutions: A Useful Tool for Seismotectonics*, S. D'Amico (Editor), Springer International Publishing, Cham, Switzerland, doi: 10.1007/978-3-319-77359-9_1.

Zhang, H., K. D. Koper, K. Pankow, and Z. Ge (2017). Imaging the 2016 Mw 7.8 Kaikoura, New Zealand, earthquake with teleseismic P waves: A cascading rupture across multiple faults, *Geophys. Res. Lett.* **44,** 4790–4798, doi: 10.1002/2017GL073461.

Manuscript received 12 April 2022
Published online 12 October 2022